The Astrophysical Journal, 957:27 (11pp), 2023 November 1 https://doi.org/10.3847/1538-4357/acf4f3

Simultaneous NICER and NuSTAR Observations of the Ultracompact X-Ray Binary 4U 0614+091

D. L. Moutard[1], R. M. Ludlam[1], J. A. García[2], D. Altamirano[3], D. J. K. Buisson[4], E. M. Cackett[1], J. Chenevez[5], N. Degenaar[6], A. C. Fabian[7], J. Homan[8], A. Jaodand[2], S. N. Pike[9], A. W. Shaw[10], T. E. Strohmayer[11], J. A. Tomsick[12], and B. M. Coughenour[12]

[1] Department of Physics & Astronomy, Wayne State University, 666 West Hancock St., Detroit, MI 48201, USA; david.moutard@wayne.edu
[2] Cahill Center for Astronomy and Astrophysics, California Institute of Technology, 1200 E. California Blvd., MC 290-17, Pasadena, CA 91125, USA
[3] School of Physics and Astronomy, University of Southampton, University Rd., Southampton SO17 1BJ, UK
[4] Independent Researcher, UK
[5] Department of Space Research & Technology, Technical University of Denmark, Elektrovej, 327, 214, DK- 2800 Kgs. Lyngby, Denmark
[6] Anton Pannekoek Institute for Astronomy, University of Amsterdam, Science Park 904, 1098 XH Amsterdam, The Netherlands
[7] Institute of Astronomy, University of Cambridge, Madingley Rd., Cambridge CB3 0HA, UK
[8] Eureka Scientific, 2452 Delmer Street Suite 100, Oakland, CA 94602, USA
[9] Department of Astronomy and Astrophysics, University of California, San Diego, 9500 Gilman Dr., La Jolla, CA 92093, USA
[10] Department of Physics and Astronomy, Butler University, Indianapolis, IN 46208, USA
[11] NASA Goddard Space Flight Center, 8800 Greenbelt Rd., Greenbelt, MD 20771, USA
[12] Space Sciences Lab, University of California, Berkeley, 7 Gauss Way, Berkeley, CA 94720, USA
Received 2023 June 15; revised 2023 August 17; accepted 2023 August 28; published 2023 October 23

Abstract

We present the first joint NuSTAR and NICER observations of the ultracompact X-ray binary 4U 0614+091. This source shows quasiperiodic flux variations on the timescale of ∼days. We use reflection modeling techniques to study various components of the accretion system as the flux varies. We find that the flux of the reflected emission and the thermal components representing the disk and the compact object trend closely with the overall flux. However, the flux of the power-law component representing the illuminating X-ray corona scales in the opposite direction, increasing as the total flux decreases. During the lowest flux observation, we see evidence of accretion disk truncation from roughly 6 gravitational radii to 11.5 gravitational radii. This is potentially analogous to the truncation seen in black hole low-mass X-ray binaries, which tends to occur during the low/hard state at sufficiently low Eddington ratios.

Unified Astronomy Thesaurus concepts: Accretion (14); Stellar accretion disks (1579); Neutron stars (1108); X-ray binary stars (1811); Low-mass x-ray binary stars (939)

1. Introduction

Ultracompact X-ray binaries (UCXBs) are a class of low-mass X-ray binary (LMXB) that are distinguished by a significantly shorter orbital period (<80 minutes) compared to "typical" LMXBs, which tend to have periods between a few hours to days. To achieve such a short orbital period, the compact object is likely accreting material from a degenerate companion such as a white dwarf (WD) or helium star (Nelson et al. 1986; Savonije et al. 1986). These objects are persistent gravitational wave sources that could be of interest to future multimessenger missions (Chen et al. 2020). They are also, more generally, probes of WD physics, accretion physics, and the physics of compact objects.

In LMXB systems, X-rays are believed to originate from near the compact object, from the closest accretion inflow. The source of high-energy nonthermal photons is thought to be an X-ray corona, which is located very near the compact object itself (Syunyaev et al. 1991). This corona of hot, highly accelerated electrons Compton upscatter seed photons from the disk or boundary layer, producing hard X-ray emission (Ibragimov et al. 2005). These X-rays can be viewed directly by observers, but they can also be reprocessed by regions in the disk. In many LMXBs, these reprocessed features commonly appear as an Fe Kα feature around 6.4 keV (Fabian et al. 1989). Because of the oxygen-rich WD companion in some UCXBs, the accretion disks are often devoid of hydrogen and helium (Nelemans et al. 2004, 2006), while the reflection spectrum displays an O VIII Lyα line around 0.67 keV (Christian et al. 1994; Juett et al. 2001).

X-ray reflection modeling is a technique used to model the photons that are reprocessed by the disk. By combining a continuum model with an X-ray reflection model, we can study the properties of the accretion disk and the X-ray source. The continuum portion of the model accounts for direct emission from the disk, corona, and the compact object itself. The reflected emission is broadened by Doppler, special, and general relativistic effects. Hence, the degree of broadening in the reflection spectrum is correlated to the proximity to the compact object, yielding measurements of the inner disk radius. This technique has been used to constrain accretion disk parameters for many LMXBs and a handful of UCXBs (Miller 2007; Cackett et al. 2008, 2009b, 2010; Madej et al. 2014; Ludlam et al. 2021). In this paper, we use simultaneous data from both NICER (Gendreau et al. 2012) and NuSTAR (Harrison et al. 2013), and we model the reflection spectra and probe the accretion disk of the UCXB 4U 0614+091.

4U 0614+091 was originally detected as an X-ray burster in 1975 (Swank et al. 1978). The presence of Type-I X-ray bursts has identified the compact source as a neutron star (NS; Brandt

Table 1
4U 0614+091 Observation Information

Obs.	Mission	Sequence ID	Obs. Start (UTC)	Exp. (ks)
1	NuSTAR	30702009002	2021-10-06 05:36:09	28.7
	NICER	4701010101	2021-10-06 06:05:29	15.3
2	NuSTAR	30702009004	2021-10-09 09:16:09	29.4
	NICER	4701010201	2021-10-09 08:06:17	21.1
	...	4701010202	2021-10-09 23:37:04	2.1
3	NuSTAR	30702009006	2021-10-11 17:41:09	29.0
	NICER	4701010301	2021-10-11 17:27:39	7.6
	...	4701010302	2021-10-11 23:35:00	11.6
4	NuSTAR	30702009008	2021-10-13 17:56:09	28.6
5	NuSTAR	30702009010	2022-01-19 06:51:09	28.2
	NICER	4701010401	2022-01-19 07:07:18	10.4

et al. 1992), and the presence of oxygen and neon features indicates that the donor source is likely a WD (Juett et al. 2001; Nelemans et al. 2004). The orbital period of the system is approximately 50 minutes (Shahbaz et al. 2008). Previous spectral studies have shown evidence of both O VIII and Fe K reflection features in the system (Madej et al. 2010, 2014; Ludlam et al. 2019), and found that the Fe abundance is subsolar. Migliari et al. (2010) combined spectral data ranging from radio to X-ray, providing the first detection of the radio counterpart and characterizing the jet in the system. Using XMM-Newton and XILLVERCO (a reflection table with abundances matching those of a WD), Madej et al. (2014) studied 4U 0614+091 and found that XILLVERCO improved reflection fit statistics by ∼16% over previous reflection models, and verified the existence of absorption edges around 0.88 keV.

The long-term light curve for this object is variable and displays quasiperiodic behavior, peaking every few days. By studying the spectral changes over various phases of this light curve, we can study which components drive the changing flux, and whether the location of the inner accretion disk radius varies in response. This paper is divided as follows: In the next section, we discuss the observations and data reduction. In Section 3 we discuss the modeling methods used and share our results. In Section 4 we discuss the implications of these results, and then finally in Section 5 we summarize these results and conclude.

2. Observations and Data Reduction

The source was observed on five occasions with NuSTAR, four of which were performed simultaneously with NICER. Table 1 provides the observing details for the contemporaneous NICER and NuSTAR observations. The NuSTAR data were reduced using the standard data reduction process with NUSTARDAS v2.1.2 and CALDB 20221115. Spectra and light curves were extracted using a circular region with a 160″ diameter centered on the source. Backgrounds were generated from a 160″ diameter region on the same detector but away from the source. The NICER observations were reduced using NICERDAS 2022-10-20_V010. Data were recalibrated with the latest calibration files available in CALDB release 20221001 through the implementation of the NICERL2 command. Good time intervals (GTIs) were generated using NIMAKETIME to select events that occurred when the particle background was low (KP < 5 and COR_SAX > 4) and avoiding times of extreme optical light loading. The GTIs were applied to the data with NIEXTRACT-EVENTS. If two NICER observations occurred during the NuSTAR observation, the GTIs were combined with FTMGTIME. The resulting event files were loaded into XSELECT to extract light curves in various energy bands. Source and background spectra were generated using the nibackgen3C50 tool (Remillard et al. 2022) for each cleaned and calibrated but unfiltered (ufa) event file pair based on instrument proxies to account for the observing conditions at the time. Spectral response files were generated via NICERARF and NICERRMF.

There were no Type-I X-ray bursts present in either data set; therefore, no further filtering was needed. Systematic errors of 1% in the full 0.3–10 keV band were added to the NICER spectrum. Both the NICER and the NuSTAR spectra were binned using the optimal binning scheme (Kaastra & Bleeker 2016) with a requirement of at least 30 counts per bin to ensure the use of χ^2 statistics. Figure 1 shows the NuSTAR and NICER light curves binned to 128 s for each observation. We show in Figure 2 the hardness ratio in two energy bands for NICER (2.0–3.8 keV / 1.1–2.0 keV and (3.8–6.8 keV / 1.1–2.0 keV) versus the 0.5–6.8 keV intensity of 4U 0614+091, as well as the hardness ratio (10 − 16 keV / 6.4–10 keV) versus intensity from the NuSTAR band.

3. Spectral Modeling and Results

In this section, we describe the modeling techniques we use. We begin by modeling just the continuum, then we include DISKLINE model components to attempt to account for the reflection features. After that, we replace the DISKLINE components with XILLVERCO, and then we refine the use of XILLVERCO by tying certain parameters and fitting the data simultaneously.

3.1. Continuum Modeling

We initially model the continuum with an absorbed three-component model CRABCOR*EDGE*EDGE*TBABS*(BBODY + DISKBB + POWERLAW). CRABCOR is comprised of a multiplicative constant and a term $E^{-\Delta\Gamma}$ as done by Steiner et al. (2010). This component aligns the amplitudes and slopes between NICER and NuSTAR data in order to account for the mission-specific calibration differences. The constant is held at 1 for the FPMA spectrum in NuSTAR. The $\Delta\Gamma$ component is fixed to zero for both FPMA and FPMB NuSTAR spectra and allowed to vary in NICER to align the slopes. The two edge components account for absorption edge features at low energies—one at ∼0.42 keV and the other at ∼0.86 keV—similar to those used in Ludlam et al. (2020). These absorption edges are likely astrophysical in origin, but we defer to previous studies that use EDGE in their analyses. TBABS is a model component that accounts for absorption by the interstellar medium (ISM) along the line of sight. For TBABS, we use the WILM abundance (Wilms et al. 2000) and the VERN cross section (Verner et al. 1996). The three additive components BBODY + DISKBB + POWERLAW account for thermal emission from the NS, thermal emission from the disk, and nonthermal emission from the corona, respectively.

With the model in place, we use XSPEC v.12.12.1 (Arnaud 1996) to fit each observation with the continuum. The initial fit is then used as a starting position for a Markov Chain Monte Carlo (MCMC) fit. The chains are comprised of 100 walkers, with a burn-in period of 500,000 steps before a

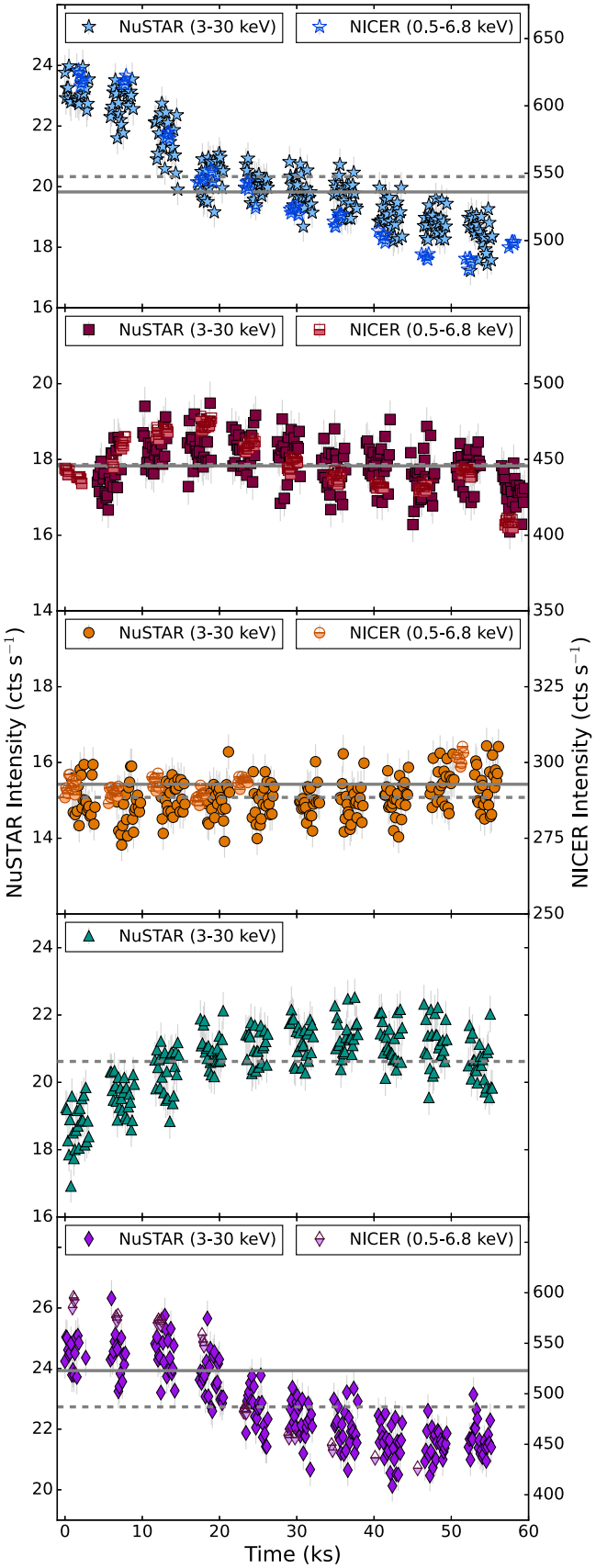

Figure 1. Light curve for the NuSTAR/FPMA and NICER observations of 4U 0614+091 binned to 128 s. Each panel represents a unique observation epoch, which is indicated by the unique symbols in each plot. The gray dashed and solid lines indicate the average count rate for NuSTAR and the NICER, respectively. Only one focal plane module is shown for clarity.

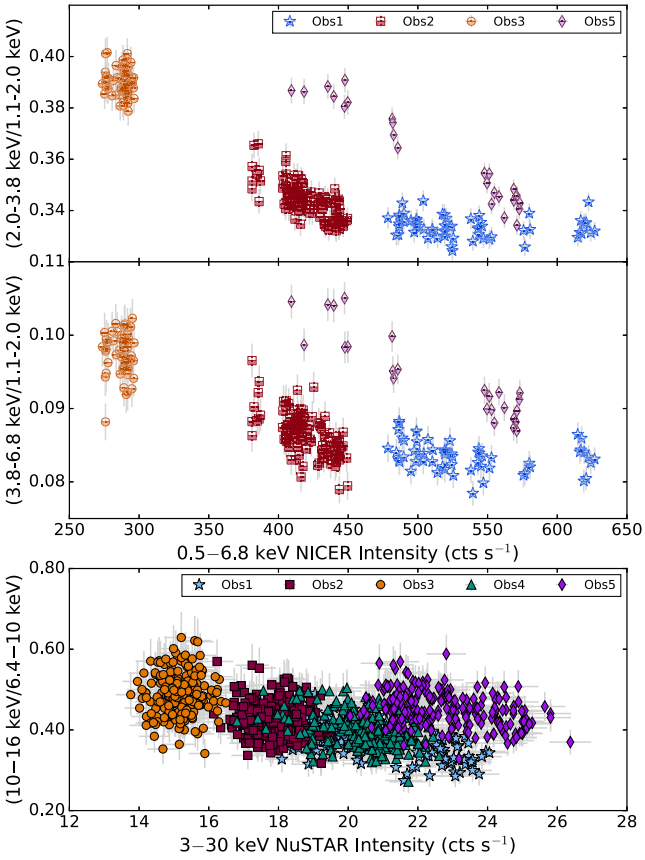

Figure 2. The hardness-intensity diagrams for different NICER and NuSTAR energy bands for each joint observation of 4U 0614+091. The top two panels are constructed from NICER data while the bottom panel is NuSTAR.

chain of 25,000 steps. The results of this fit are displayed in Table 2. Although the data are binned to a minimum number of counts per bin to allow the use of χ^2 statistics, the "standard" weighting scheme in XSPEC often resulted in overfitting the data, yielding a reduced $\chi^2 < 1$. This is a known issue discussed in Galloway (2020) regarding the handling of the low-count bins in XSPEC v.12. We therefore switch to the "Churazov" weighting scheme when performing our spectral fits and report the values for the χ^2/degree of freedom (dof) in Tables 2–5. Churazov weighting adjusts the weight by averaging the counts in surrounding channels, which can smooth the overall weighting and not apply disproportionate weight to local extrema (Churazov et al. 1996). All errors are reported at the 90% level.

As can be seen in Table 2, observation 4 used a simplified version of the model. Since no NICER data are available, CRABCOR is replaced with a simple CONST term to align the FPMA and FPMB of NuSTAR. In initial runs, attempting to use the full model resulted in poor constraints on parameters. This is due to the fact that much of the model information is primarily seen in the NICER region of the spectrum. This includes both edge components and most of the absorption covered by TBABS. For example, the DISKBB peak is always found to be <0.7 keV. An early fit using DISKBB had values for kT=$0.35^{+0.34}_{-0.04}$ keV and the normalization component was completely unconstrained, without any improvement in the χ^2/dof. Observation 4 is well modeled by a very simple continuum, with a χ^2/dof ≈1.14. As a result of this, we will not consider it for most of the remaining analysis.

Table 2
Continuum Model, Individual Fit

Model Component	Parameter	Obs1	Obs2	Obs3	Obs4	Obs5
CRABCOR	C_{FPMB} (10^{-1})	10.00 ± 0.04	9.97 ± 0.04	$9.89^{+0.04}_{-0.05}$	10.02 ± 0.04	9.82 ± 0.04
	C_{NICER} (10^{-1})	$9.3^{+0.2}_{-0.1}$	9.7 ± 0.2	$9.1^{+0.3}_{-0.2}$	⋯	$9.1^{+0.3}_{-0.1}$
	$\Delta\Gamma$ (10^{-2})	$-3.8^{+1.2}_{-1.8}$	$1.0^{+1.3}_{-1.6}$	$-2.5^{+2.5}_{-1.1}$	⋯	$-4.2^{+2.3}_{-1.0}$
EDGE	E (10^{-1} keV)	4.42 ± 0.01	4.33 ± 0.01	4.54 ± 0.01	⋯	4.44 ± 0.01
	τ_{max}	2.8 ± 0.1	2.3 ± 0.1	$2.3^{+0.2}_{-0.1}$	⋯	3.5 ± 0.1
EDGE	E (10^{-1} keV)	8.62 ± 0.01	8.63 ± 0.01	8.49 ± 0.02	⋯	$8.63^{+0.01}_{-0.02}$
	τ_{max} (10^{-1})	4.4 ± 0.1	$4.30^{+0.05}_{-0.04}$	3.0 ± 0.1	⋯	4.1 ± 0.1
TBABS	N_H (10^{21} cm^{-2})	2.3 ± 0.1	0.17 ± 0.01	0.07 ± 0.02	⋯	$0.011^{+0.004}_{-0.001}$
BBODY	kT (keV)	1.24 ± 0.01	1.20 ± 0.02	1.24 ± 0.04	$1.20^{+0.02}_{-0.01}$	$1.13^{+0.02}_{-0.01}$
	$norm_{bb}$ (10^{-3})	2.5 ± 0.1	1.1 ± 0.1	0.8 ± 0.1	1.8 ± 0.1	1.7 ± 0.1
DISKBB	kT (keV)	$0.427^{+0.004}_{-0.007}$	0.32 ± 0.01	$0.64^{+0.02}_{-0.01}$	⋯	0.45 ± 0.01
	$norm_{dbb}$	731^{+61}_{-38}	1088^{+159}_{-140}	74^{+6}_{-11}	⋯	421^{+30}_{-60}
POWERLAW	Γ	$2.31^{+0.02}_{-0.01}$	2.29 ± 0.01	1.94 ± 0.02	2.30 ± 0.01	2.10 ± 0.01
	$norm_{pl}$ (10^{-1})	$3.2^{+0.2}_{-0.1}$	3.3 ± 0.1	1.4 ± 0.1	3.6 ± 0.1	2.8 ± 0.1
	χ^2 (dof)	2410 (407)	3705 (410)	954 (405)	374 (273)	1264 (406)

Note. Errors are given at the 90% level. The BBODY normalization is defined as $(L/10^{39}$ erg s$^{-1})/(D/10$ kpc$)^2$, the DISKBB normalization is defined as $(R_{in}/$ km$)^2/(D/10$ kpc$)^2 \times \cos\theta$, and the POWERLAW normalization is defined as photons keV^{-1} cm^{-2} s^{-1} at 1 keV.

Table 3
Diskline Model, Individual

Model Component	Parameter	Obs1	Obs2	Obs3	Obs5
CRABCOR	C_{FPMB} (10^{-1})	$9.99^{+0.05}_{-0.03}$	9.98 ± 0.04	$9.85^{+0.08}_{-0.02}$	$9.84^{+0.03}_{-0.04}$
	C_{NICER} (10^{-1})	$8.5^{+0.1}_{-0.2}$	$8.9^{+0.2}_{-0.3}$	$9.0^{+0.2}_{-0.3}$	$9.0^{+0.2}_{-0.3}$
	$\Delta\Gamma$ (10^{-2})	$-7.5^{+1.1}_{-1.5}$	$-4.7^{+1.3}_{-1.9}$	$-2.6^{+1.5}_{-2.2}$	$-5.6^{+1.9}_{-2.0}$
EDGE	E (10^{-1} keV)	$3.5^{+0.6}_{-0.5}$	$4.1^{+0.2}_{-0.3}$	$3.3^{+0.3}_{-0.1}$	$4.61^{+0.03}_{-1.43}$
	τ_{max}	$0.6^{+0.3}_{-0.2}$	$0.9^{+0.2}_{-0.1}$	0.6 ± 0.1	$1.0^{+1.1}_{-0.1}$
EDGE	E (10^{-1} keV)	8.98 ± 0.03	$8.97^{+0.03}_{-0.02}$	$8.79^{+0.07}_{-0.04}$	$8.93^{+0.06}_{-0.02}$
	τ_{max} (10^{-1})	$1.93^{+0.17}_{-0.05}$	2.1 ± 0.1	$1.32^{+0.08}_{-0.03}$	$2.3^{+0.1}_{-0.2}$
TBABS	N_H(10^{21} cm^{-2})	3.3 ± 0.1	$2.63^{+0.12}_{-0.04}$	2.6 ± 0.1	$2.3^{+0.5}_{-0.1}$
BBODY	kT (keV)	$1.21^{+0.01}_{-0.02}$	1.07 ± 0.02	$1.04^{+0.03}_{-0.04}$	$1.05^{+0.01}_{-0.04}$
	$norm_{bb}$ (10^{-3})	$2.52^{+0.03}_{-0.19}$	$1.58^{+0.03}_{-0.16}$	0.8 ± 0.1	1.5 ± 0.1
DISKBB	kT (keV)	$0.426^{+0.004}_{-0.008}$	$0.408^{+0.004}_{-0.008}$	0.59 ± 0.01	$0.417^{+0.003}_{-0.024}$
	$norm_{dbb}$	950^{+74}_{-39}	730^{+59}_{-60}	96^{+16}_{-12}	639^{+176}_{-4}
POWERLAW	Γ	$2.29^{+0.02}_{-0.01}$	$2.189^{+0.027}_{-0.003}$	1.96 ± 0.02	$2.12^{+0.02}_{-0.01}$
	$norm_{pl}$ (10^{-1})	$3.1^{+0.2}_{-0.1}$	$2.52^{+0.19}_{-0.02}$	1.5 ± 0.1	$2.9^{+0.2}_{-0.1}$
DISKLINEE_1	E_{line} (keV)	0.67 ± 0.01	$0.692^{+0.001}_{-0.004}$	$0.686^{+0.004}_{-0.005}$	$0.649^{+0.003}_{-0.007}$
	$\lvert q\rvert$	2.5 ± 0.1	$2.36^{+0.06}_{-0.02}$	$2.22^{+0.10}_{-0.03}$	$2.4^{+0.4}_{-0.2}$
	R_{in} (R_g)	$6.4^{+0.8}_{-0.4}$	$6.05^{+0.29}_{-0.05}$	$6.3^{+2.6}_{-0.3}$	$6.2^{+0.1}_{-0.2}$
	norm (10^{-2} keV)	$7.3^{+0.6}_{-0.7}$	$4.2^{+0.4}_{-0.1}$	1.5 ± 0.1	$4.8^{+0.6}_{-0.2}$
	EW (eV)	63^{+1}_{-7}	49^{+4}_{-1}	34^{+2}_{-3}	47^{+2}_{-5}
DISKLINEE_2	E_{line} (keV)	$6.44^{+0.08}_{-0.21}$	$6.59^{+0.07}_{-0.16}$	6.7 ± 0.1	$6.3^{+0.1}_{-0.2}$
	norm (10^{-4} keV)	$3.8^{+1.5}_{-0.4}$	5.0 ± 1.0	$3.5^{+0.5}_{-0.4}$	7.0 ± 1.0
	EW (eV)	70^{+10}_{-20}	92^{+25}_{-3}	90^{+20}_{-10}	120^{+20}_{-10}
	χ^2 (dof)	862 (401)	862 (404)	481 (399)	665 (400)

Note. Errors are given at the 90% level. The BBODY normalization is defined as $(L/10^{39}$ erg s$^{-1})/(D/10$ kpc$)^2$, the DISKBB normalization is defined as $(R_{in}/$ km$)^2/(D/10$ kpc$)^2 \times \cos\theta$, the POWERLAW normalization is defined as photons keV^{-1} cm^{-2} s^{-1} at 1 keV, and the DISKLINE normalization is defined as photons cm^{-2} s^{-1}.

Our continuum model does not provide a very good fit to observations 1–3 and 5, as is apparent from the reduced χ^2 values in Table 2, and strong residuals are seen in the Fe K and O VIII regions. The shape of the line profiles in the residuals can be seen in Figure 3. These are extracted by first ignoring the regions surrounding the O VIII (0.60–0.80 keV) and Fe K (5.5–7.4 keV) features to avoid biasing the continuum fit. The continuum is then fit. The ignored regions are then reapplied to the spectrum to demonstrate that the continuum model is insufficient to encompass the reprocessed emission and another component is necessary to fully describe the X-ray spectrum.

Table 4
Reflection Model Fits, Individual

Model Component	Parameter	Obs1	Obs2	Obs3	Obs5
CRABCOR	$C_{FPMB}(10^{-1})$	$9.99^{+0.05}_{-0.04}$	$9.99^{+0.02}_{-0.06}$	$9.88^{+0.06}_{-0.03}$	$9.84^{+0.03}_{-0.05}$
	$C_{NICER}(10^{-1})$	$8.8^{+0.4}_{-0.1}$	$8.6^{+0.3}_{-0.1}$	$8.9^{+0.3}_{-0.2}$	$8.6^{+0.2}_{-0.3}$
	$\Delta\Gamma$ (10^{-2})	$-5.2^{+2.6}_{-0.7}$	$-7.2^{+2.0}_{-1.0}$	$-3.5^{+2.2}_{-1.6}$	$-8.3^{+1.5}_{-1.8}$
EDGE	E $(10^{-1}$ keV)	$4.2^{+0.2}_{-0.9}$	$4.2^{+0.2}_{-0.4}$	$3.6^{+1.0}_{-0.5}$	$4.20^{+0.4}_{-0.7}$
	τ_{max}	$0.4^{+0.4}_{-0.1}$	0.8 ± 0.1	0.5 ± 0.2	$0.50^{+0.44}_{-0.08}$
EDGE	E $(10^{-1}$ keV)	$8.60^{+0.05}_{-0.03}$	$8.68^{+0.03}_{-0.02}$	$8.55^{+0.08}_{-0.03}$	$8.69^{+0.02}_{-0.05}$
	τ_{max} (10^{-1})	$2.0^{+0.1}_{-0.2}$	2.9 ± 0.1	$1.3^{+0.2}_{-0.1}$	$2.6^{+0.2}_{-0.1}$
TBABS	N_H $(10^{21}$ cm$^{-2})$	$3.5^{+0.2}_{-0.1}$	3.4 ± 0.1	$3.3^{+0.1}_{-0.2}$	$3.5^{+0.1}_{-0.2}$
BBODY	kT (keV)	1.09 ± 0.02	1.13 ± 0.02	$0.77^{+0.04}_{-0.06}$	$1.09^{+0.01}_{-0.05}$
	$norm_{bb}$ (10^{-3})	$2.1^{+0.2}_{-0.1}$	1.1 ± 0.1	0.7 ± 0.1	0.9 ± 0.1
DISKBB	kT (keV)	0.40 ± 0.01	0.36 ± 0.01	$0.50^{+0.02}_{-0.03}$	0.37 ± 0.01
	$norm_{dbb}$	1545^{+98}_{-92}	926 ± 67	131^{+39}_{-27}	832^{+144}_{-88}
POWERLAW	Γ	$2.07^{+0.03}_{-0.06}$	$2.33^{+0.01}_{-0.02}$	2.05 ± 0.01	$2.25^{+0.01}_{-0.02}$
	$norm_{pl}$ (10^{-1})	$0.6^{+0.1}_{-0.3}$	3.0 ± 0.1	1.6 ± 0.1	$3.6^{+0.1}_{-0.2}$
RELCONV	q	$2.5^{+0.2}_{-0.1}$	2.6 ± 0.6	2.4 ± 0.2	2.6 ± 0.1
	R_{in} (R_{ISCO})	$1.04^{+0.32}_{-0.04}$	$1.03^{+0.13}_{-0.03}$	$1.5^{+0.3}_{-0.5}$	$1.03^{+0.16}_{-0.03}$
$XILLVER_{CO}$	A_{CO}	$36.0^{+3.9}_{-2.9}$	$19.5^{+2.5}_{-2.4}$	$11.0^{+3.9}_{-1.9}$	$21.1^{+0.3}_{-5.9}$
	kT_{bb} $(10^{-2}$ keV)	$9.9^{+0.1}_{-0.4}$	$5.67^{+0.43}_{-0.07}$	$5.8^{+0.3}_{-0.2}$	$5.45^{+0.32}_{-0.02}$
	Frac (10^{-1})	$2.4^{+0.4}_{-0.2}$	$0.14^{+0.01}_{-0.02}$	0.4 ± 0.1	$0.16^{+0.02}_{-0.03}$
	norm (10^{-9})	$2.0^{+0.3}_{-0.2}$	$209.2^{+14.4}_{-53.8}$	$27.3^{+6.1}_{-5.5}$	$250.7^{+27.7}_{-64.0}$
	log(ξ)(erg cm/s)	3.5 ± 0.1	1.3 ± 0.1	1.7 ± 0.1	1.3 ± 0.1
	χ^2 (dof)	647 (401)	796 (404)	442 (399)	461 (420)

Note. Errors are given at the 90% level. The BBODY normalization is defined as $(L/10^{39}$ erg s$^{-1})/(D/10$ kpc$)^2$, the DISKBB normalization is defined as $(R_{in}/$ km$)^2/(D/10$ kpc$)^2 \times \cos\theta$, and the POWERLAW normalization is defined as photons keV^{-1} cm^{-2} s^{-1} at 1 keV.

Table 5
Reflection Model, Combined

Model Component	Parameter	Obs1	Obs2	Obs3	Obs5
CRABCOR	C_{FPMB} (10^{-1})	10.00 ± 0.01	$9.971^{+0.004}_{-0.005}$	9.90 ± 0.02	$9.828^{+0.003}_{-0.009}$
	C_{NICER} (10^{-1})	9.12 ± 0.01	$9.134^{+0.006}_{-0.003}$	9.02 ± 0.01	9.29 ± 0.01
	$^{\dagger}\Delta\Gamma$ (10^{-2})		$-2.975^{+0.004}_{-0.011}$		
EDGE	†E $(10^{-1}$ keV)		$4.10^{+0.05}_{-0.02}$		
	$^{\dagger}\tau_{max}(10^{-1})$		$3.55^{+0.02}_{-0.13}$		
EDGE	†E $(10^{-1}$ keV)		$8.720^{+0.007}_{-0.004}$		
	$^{\dagger}\tau_{max}$ (10^{-1})		$1.661^{+0.008}_{-0.002}$		
TBABS	N_H † $(10^{21}$ cm$^{-2})$		3.27 ± 0.01		
BBODY	kT $(10^{-1}$ keV)	10.76 ± 0.01	9.20 ± 0.01	$8.01^{+0.03}_{-0.05}$	$9.55^{+0.01}_{-0.05}$
	$norm_{bb}$ (10^{-3})	$2.829^{+0.012}_{-0.002}$	$1.59^{+0.01}_{-0.02}$	0.50 ± 0.01	$1.640^{+0.007}_{-0.003}$
DISKBB	kT $(10^{-1}$ keV)	4.230 ± 0.003	$3.803^{+0.003}_{-0.009}$	$5.09^{+0.03}_{-0.02}$	$3.93^{+0.01}_{-0.02}$
	$norm_{dbb}$	1347^{+8}_{-4}	1391^{+11}_{-3}	113^{+3}_{-4}	1071^{+27}_{-8}
POWERLAW	Γ	$1.912^{+0.001}_{-0.003}$	$1.963^{+0.003}_{-0.001}$	$2.059^{+0.003}_{-0.001}$	$1.991^{+0.002}_{-0.004}$
	$norm_{pl}$ (10^{-2})	$1.44^{+0.03}_{-0.01}$	5.1 ± 0.1	$17.9^{+0.2}_{-0.1}$	$14.2^{+0.1}_{-0.3}$
RELCONV	q	$2.695^{+0.010}_{-0.005}$	$2.672^{+0.009}_{-0.004}$	$2.72^{+0.02}_{-0.01}$	$2.728^{+0.004}_{-0.003}$
	R_{in} (R_{ISCO})	$1.01^{+0.04}_{-0.01}$	$1.003^{+0.038}_{-0.003}$	$1.92^{+0.05}_{-0.04}$	1.04 ± 0.01
$XILLVER_{CO}$	† A_{CO}		$25.70^{+0.27}_{-0.07}$		
	kT_{bb} $(10^{-2}$ keV)	$7.985^{+0.050}_{-0.008}$	$6.22^{+0.01}_{-0.03}$	$6.51^{+0.09}_{-0.16}$	$5.89^{+0.09}_{-0.02}$
	Frac (10^{-1})	$5.07^{+0.02}_{-0.11}$	$5.85^{+0.10}_{-0.02}$	0.49 ± 0.01	$4.63^{+0.07}_{-0.14}$
	norm (10^{-9})	$2.27^{+0.01}_{-0.02}$	$3.46^{+0.03}_{-0.04}$	$6.8^{+0.7}_{-0.4}$	$4.4^{+0.1}_{-0.2}$
	log(ξ)$(ergcm/s)$	3.42 ± 0.01	3.05 ± 0.01	2.05 ± 0.02	2.86 ± 0.02
Ccolspan1-6					
	χ^2 (dof)		2593 (1625)		

Note. Errors are given at the 90% level. The BBODY normalization is defined as $(L/10^{39}$ erg s$^{-1})/(D/10$ kpc$)^2$, the DISKBB normalization is defined as $(R_{in}/$ km$)^2/(D/10$ kpc$)^2 \times \cos\theta$, and the POWERLAW normalization is defined as photons keV^{-1} cm^{-2} s^{-1} at 1 keV. †: Tied parameters.

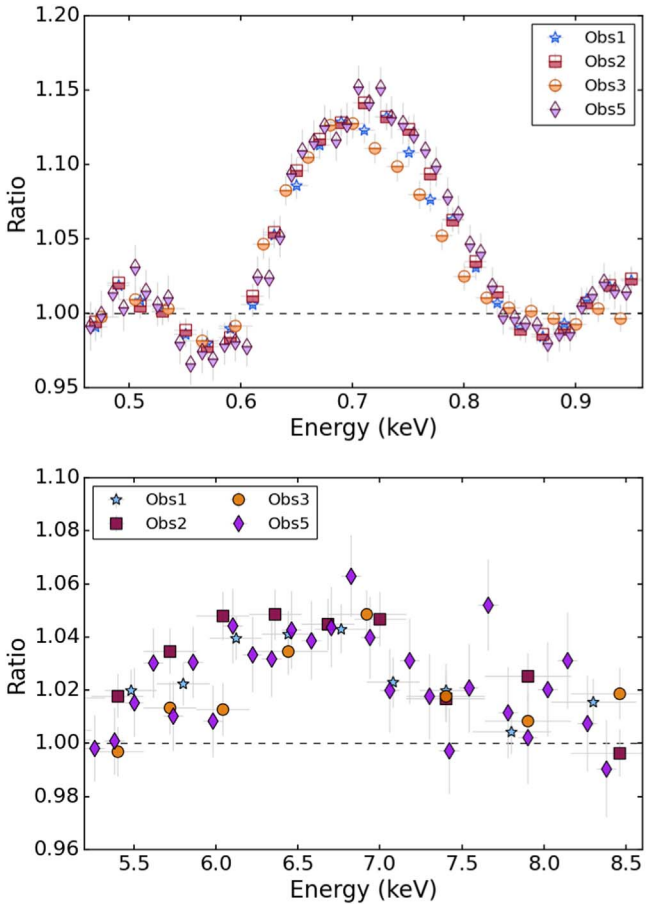

Figure 3. (Top) O VIII Lyα line profile from NICER for observations 1, 2, 3, and 5 centered at ~0.7 keV. (Bottom) Fe Kα profile from FPMA in NuSTAR centered at ~6.5 keV. The Fe features are notably weaker than the O VIII features, with the former peaking at around 6% above the continuum, and the latter peaking at around 15% above the continuum.

3.2. Modeling the Reprocessed Emission

As an initial test of the strength of the reflected line features, we include two DISKLINE components, centered near 0.67 keV and 6.5 keV. DISKLINE is a model component that accounts for a single line emission feature from a relativistically blurred disk. The equivalent width (EW) of each line is measured using the EQWIDTH command in XSPEC. In addition to estimating the EW, we also test the location of these features within the disk since the O VIII Lyα and Fe Kα features could arise from separate radii. However, due to the lower signal-to-noise of the Fe Kα line, the location of that feature is poorly constrained. The lower limit on the emission radius is 6 gravitational radii ($R_g = GM/c^2$) in each case, consistent with the O VIII feature. We therefore tie the values of the emission radius $R_{\rm in}$ for both line components in the fit, the results of which can be found in Table 3.

To model the reprocessed emission, we utilize RELCONV*-XILLVERCO. XILLVERCO is a version of XILLVER, an additive component for XSPEC, which is a table of synthetic reflected spectra (García & Kallman 2010; García et al. 2013) that has been developed with the unique features of UCXBs in mind, by including an overabundance of the carbon and oxygen expected from a WD companion (Madej et al. 2014). RELCONV is a relativistic blurring kernel used to account for the strong gravity close to the NS and Doppler broadening effects.

In RELCONV, the two emissivity indices q_1 and q_2 for the inner and outer disk are tied and reported as q, and so the radius R_{br} at which these indices differ becomes obsolete. The outer radius is fixed at 990 R_g, and the inner disk radius $R_{\rm in}$ in units of $R_{\rm ISCO}$ (1 $R_{\rm ISCO} = 6\,R_g$ for spin $a = 0$) is free to vary. The limb, spin, and redshift parameters are all fixed at zero. In XILLVERCO, we tie the value of Γ to the power-law index of the continuum power-law component as this is the illuminating input source of the reprocessed emission in the model. The carbon and oxygen abundance A_{CO} is measured in units of solar abundance, and the value denoted as Frac is the measured ratio of the illuminating power-law flux to the flux of the emergent blackbody. The normalization of XILLVERCO is defined such that an incident spectrum with flux $F(E)$ follows the expression

$$\int_{0.1\ \rm keV}^{1\ \rm MeV} F(E)dE = \frac{10^{35}}{4\pi}\ \rm erg\ cm^4\ s^{-1} \quad (1)$$

(Dauser et al. 2016). The inclination of the system is fixed at 55° because of the high number of free variables. This value is consistent with the inclinations measured by Madej et al. (2014) and Ludlam et al. (2019). We test that our results are not dependent upon this choice of fixed inclination by running fits with the inclination tied across observations but free to vary. The inclination remains consistent at 55°. We find that all key parameters of interest are consistent within the 90% confidence level to the fits with fixed inclination. Therefore, our results are robust with respect to inclination and we only report on the fits with this parameter fixed.

Initially, the model is fit to each observation, using the same methods as discussed in Section 3.1. Once fit, the ionization parameter ξ of the system is calculated with the value of Frac and the disk temperature kT from XILLVERCO using:

$$\xi = \frac{4\pi}{n}F_x, \quad (2)$$

where $F_x = \rm Frac \times \sigma T^4$, defined using the blackbody temperature, and Frac as defined in XILLVERCO. Note that the blackbody temperature from XILLVERCO differs from the disk temperature in DISKBB in that it represents the region of the disk where reflection occurs versus the emission of the entire disk as measured by DISKBB. DISKBB is a multitemperature blackbody representing emission from the entire disk, whereas the thermal temperature included in XILLVERCO only accounts for disk emission at the radius at which the O line originates.[13] The final value is reported in log units. Here, n is the disk number density that is a fixed value of 1×10^{17} cm^{-3} in the reflection model. The results of these fits and calculations are reported in Table 4.

After fitting each observation individually with the aforementioned models, we simultaneously fit all observations, tying components that should remain consistent over time. These consistent variables are the hydrogen column density N_H, the absorption edge components, the slope difference between NuSTAR and NICER $\Delta\Gamma$, and the carbon–oxygen abundance A_{CO}. With these parameters tied, we repeat the same process as before and report the results in Table 5. Compared to the continuum model without accounting for relativistically broadened reflection features, the $\chi^2/$ dof improves greatly.

[13] See Madej et al. (2014) for further discussion.

We also measure the unabsorbed flux of each component between 0.5 and 50 keV as the system varies. This range is chosen to be consistent with Ludlam et al. (2019) to allow for direct comparison to other accreting sources. The trends for the blackbody, disk blackbody, and reflected emission follow the same trend of the overall flux. The power-law flux representing the coronal emission, however, seems to vary in the opposite direction, increasing in flux as the overall flux decreases, as shown in Figure 4. These values are reported in Table 6.

Across each observation, $R_{\rm in}$ is consistent with 1 $R_{\rm ISCO}$. The exception is in the lowest flux observation, Obs3, for which the disk appears to recede to $1.92R_{\rm ISCO}$. To statistically test this result, we repeat the fit in Table 5, but this time we fix $R_{\rm in}$ to $1R_{\rm ISCO}$. The quality of the overall fit worsens by 3.9σ ($\Delta\chi^2 = 15$ worse for 1 dof), hence the disk truncation is required by the data. Over the course of the observations, the blackbody temperature and $\log(\xi)$ correlates with the overall flux, increasing as the flux of the system increases and vice versa. The temperature of the disk shows no such correlation, remaining relatively constant across the observations 1, 2, and 5, but increases significantly during our lowest flux observation. This contributes to the increased hardness during Obs3.

We also recognize that the low disk normalization and high disk temperature of Obs3 in Table 5 imply a smaller inner disk radius (4.5 km assuming $\theta = 55°$ and $D = 3.3$ kpc). Even when accounting for a spectral hardening factor, which can increase the calculated inner disk radius by a factor of $\sim$1.6 (Shimura & Takahara 1995; Lazar et al. 2021), we find the inferred inner disk radius to be far smaller than the truncated inner disk radius from RELCONV. This is possibly caused by a degeneracy between the disk and other components. We find that if we force the disk normalization to a value more consistent with the other observations, the disk temperature decreases to well below our passband and the blackbody temperature increases to a value that is much too high (e.g., it increased to roughly 9 keV in some cases). We do not assume this to be a physical parameter of the system at this observation. Additionally, we tested the use of SIMPL (Steiner et al. 2009) instead of POWERLAW to account for Comptonization in the continuum while remaining consistent with the input model of XILLVERCO in an attempt to correct for the inconsistent behavior of the DISKBB component in Obs3. This also led to a truncated disk in Obs3, though the value was poorly constrained. The fit quality was greatly reduced (with the reduced χ^2 nearly doubling); therefore, we do not report on them further.

For completeness, we also tried other model components before using those in the final table. For example, we attempted to replace TBABS*EDGE*EDGE with VARABS, a model component with variable absorption that could account for both edges as well as any other nonsolar abundance in the ISM. Tests with this component yielded results that were similar to those in the final analysis but with the added complication of greatly increasing the number of free parameters (TBVARABS has up to 42 free parameters). Because of the already large number of free parameters in the tied fits shown in Table 5, we opted to use the simpler of the two models.

4. Discussion

We perform a spectral analysis of four simultaneous NICER and NuSTAR observations of 4U 0614+091. Each observation shows the presence of disk reflection in the form of emission line features that have been relativistically broadened, indicating that they originate from the innermost disk region. We find that the disk shows evidence of truncation during Obs3. We consistently find an increase in the inner disk radius for this observation compared to the other higher flux observations. In particular, when we simultaneously fit all observations, tying parameters that should remain physically unchanged between them, Obs3 is the only instance where $R_{\rm in}$ is inconsistent with 1 $R_{\rm ISCO}$ (see Table 5).

Because we only observed one minimum during the long-term light curve, it is difficult at this time to determine whether the apparent disk truncation is correlated with the low flux state, or if it is a coincidence. However, this behavior is analogous to that seen in black hole (BH) LMXBs. In many BH LMXBs, it is expected that during the low/hard state, this type of truncation might be observed (Done et al. 2007). In these BH LMXB systems, the disk recedes at values of $L/L_{\rm Edd}$ below $\sim$0.01 (Tomsick et al. 2009). By examining the contributing fluxes of each component as shown in Figure 4, we can see that during the lowest flux state, the flux of the power-law component becomes dominant, while the thermal sources of X-rays (as well as the reflected emission) becomes a small fraction of the overall flux. Using the empirical Eddington luminosity for a 1.4 $M_\odot$ NS $L_{\rm Edd} = 3.8 \times 10^{38}$ erg s^{-1} (Kuulkers et al. 2003), we compile archival measured values (Ludlam et al. 2019, 2020; Mondal et al. 2020; Ludlam et al. 2021; Saavedra et al. 2023) for $R_{\rm in}$ for various NS LMXBs studied with NuSTAR in Figure 5 and compare to their Eddington fractions at time of observation. This figure demonstrates that, while there may be some correlation between the Eddington fraction $F_{\rm Edd}$ and $R_{\rm in}$, there is not a direct correlation for NSs, though similar behavior can be seen for the NS LMXB Ser X-1 (Chiang et al. 2016; Mondal et al. 2020). In that source, the authors report evidence of disk truncation during a low flux state. In this study, we are able to probe some of the lowest regimes of the Eddington ratio, and we find our result to be consistent with results on the same source from Ludlam et al. (2019) at the same flux as observation 1, with a major difference being the lack of NICER data in the initial study. Since NSs and BHs are both compact accretors, we might expect their behavior to be similar. This is complicated by the magnetic fields and surfaces that are present around an NS.

To test the feasibility of a disk depletion between observations 2 and 3, we calculate the mass accretion rate $\dot{M}$ using the equation

$$\dot{M} = \frac{L}{\eta c^2}, \tag{3}$$

where L is the luminosity, calculated using the unabsorbed flux between 0.5 and 50 keV at 3.3 kpc (this distance was obtained by Arnason et al. (2021) using GAIA Data Release 2), and we assume an efficiency $\eta = 0.2$. To obtain the minimum time needed to deplete the inner region between 1 and 2 $R_{\rm ISCO}$, we use the minimum measured flux for observation 3 and hence the lowest observed mass accretion rate, allowing for a more conservative estimate. We calculate a value $\dot{M} = 4.37 \times 10^{-18} M_\odot {\rm yr}^{-1}$, and then combine with the Shakura–Sunyaev disk solution for the surface density Σ to calculate the disk mass $M_{\rm disk}$ (see Frank et al. 2002 for more

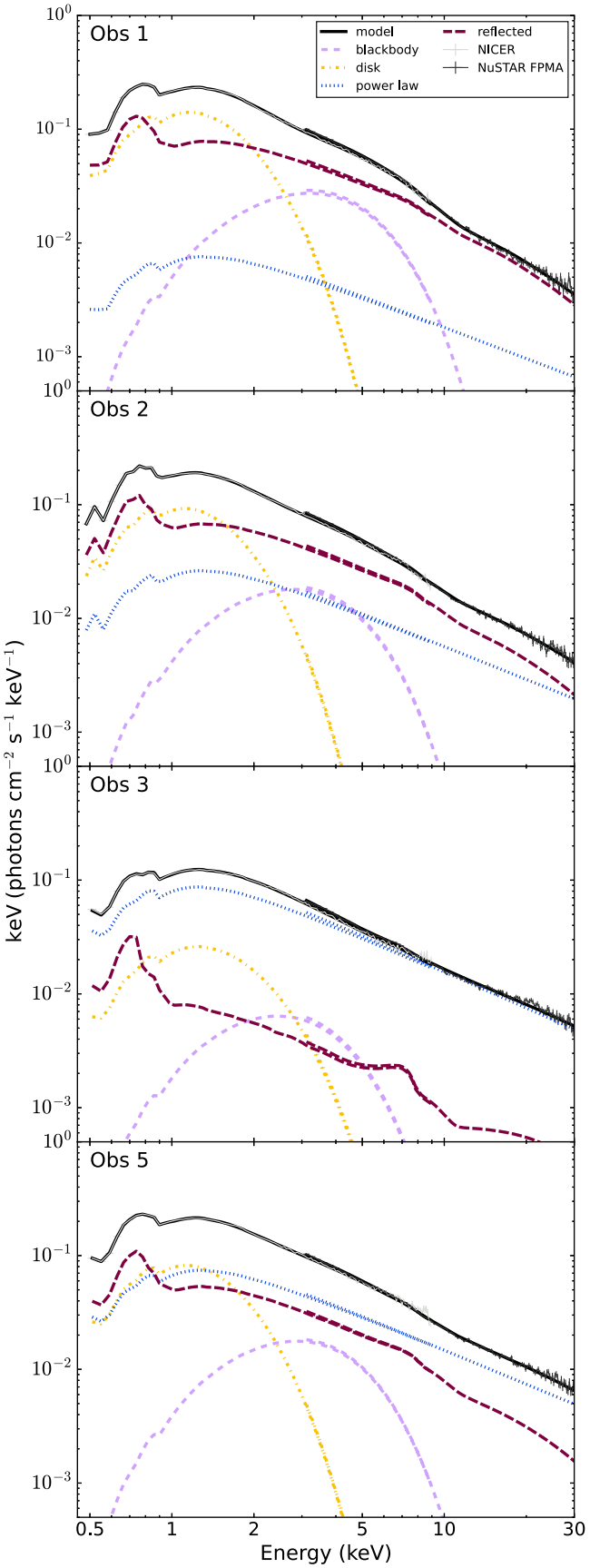

Figure 4. The unfolded spectra and model components for each observation as the flux varies. The model components shown here are those displayed in Table 5. The power law, displayed with a blue dotted line, becomes the dominant contributor to the overall spectrum during Obs3, the lowest flux state.

Table 6
Component fluxes

Model Component	Obs1	Obs2	Obs3	Obs5
Blackbody	2.4 ± 0.1	1.4 ± 0.1	0.4 ± 0.1	1.3 ± 0.1
Disk	6.4 ± 0.2	4.1 ± 0.1	1.3 ± 0.2	3.6 ± 0.2
Powerlaw	1.3 ± 0.3	4.1 ± 0.5	12.1 ± 0.3	10.8 ± 1.2
XillverCO	12.0 ± 1.0	9.8 ± 1.2	1.4 ± 2.7	7.6 ± 1.8
Total	19.5 ± 1.1	17.3 ± 1.3	13.7 ± 2.7	21.6 ± 2.2

Note. All fluxes reported have units 10^{-10} erg s^{-1} cm^{-2} and are measured in the range 0.5–50 keV. It should be noted that Obs5 occurred approximately 3 months after the first four observations.

detail):

$$M_{\rm disk} = 2\pi \int_{R_*}^{R_{\rm out}} \Sigma R dR. \quad (4)$$

We find that at this conservative $\dot{M}$, disk truncation due to a complete depletion would take far longer than the ∼2 days between observations 2 and 3 (approximately 5 yr). This implies that disk depletion is not the primary driver of truncation in this system. Instead, it may be related to a change in the transition radius between the accretion disk and the coronal flow, as discussed for BH systems in Liu et al. (1999). This is supported by an increased flux of the coronal emission during this low flux state. In Marino et al. (2020), the authors conducted a study of 4U 0614+091 and suggested that during an "extreme island state," atoll sources often have lower blackbody temperatures and truncated disks. This is consistent with what we are seeing in observation 3, where the blackbody temperature has decreased and the spectrum is harder than what is seen in the other observations. In both Marino et al. (2020) and Migliari et al. (2010), the authors discuss the coupling between the jet and the disk. Unfortunately without simultaneous radio measurements, we can not know whether this disk behavior is driven by a jet.

The disk could be truncated due to the magnetic field strength of the NS at such a low mass accretion rate. To estimate the equatorial strength of the magnetic field, we can use the following equation, as done in Ludlam et al. (2020):

$$B = 3.5 \times \quad 10^5 \, k_A^{-7/4} x^{7/4} \left(\frac{M}{1.4\ M_\odot}\right)^2 \left(\frac{10\ \rm km}{R_{\rm NS}}\right)^3 \times \left(\frac{f_{\rm ang}}{\eta} \frac{F_{\rm bol}}{10^{-9}\ \rm erg\ s^{-1} cm^{-2}}\right)^{1/2} \frac{D}{3.5\ \rm kpc}\ \rm G, \quad (5)$$

where η is assumed to be 0.2, the conversion factor k_A and the angular anisotropy $f_{\rm ang}$ are set to unity, the distance D to 4U 0614+091 is 3.3 kpc (as mentioned previously), canonical NS values are used for M and R_{NS}, and the $0.5 - 50$ keV flux and the inner disk radius (in R_g) for observation 3 are used for $F_{\rm bol}$ and x, respectively. We obtain an upper limit on the magnetic field to be $B \leqslant 0.6 \times 10^8$ G at the equator or $B \leqslant 1.2 \times 10^8$ G at the pole. The magnetosphere radius, assumed to be proportional to $\dot{M}^{-2/7}$, does not follow the measured $R_{\rm in}$, so the disk truncation is not driven primarily by the magnetosphere either, similar to what is seen in Chiang et al. (2016).

Because the model assumes that the illuminating flux is provided by the X-ray corona, the inverse relationship between

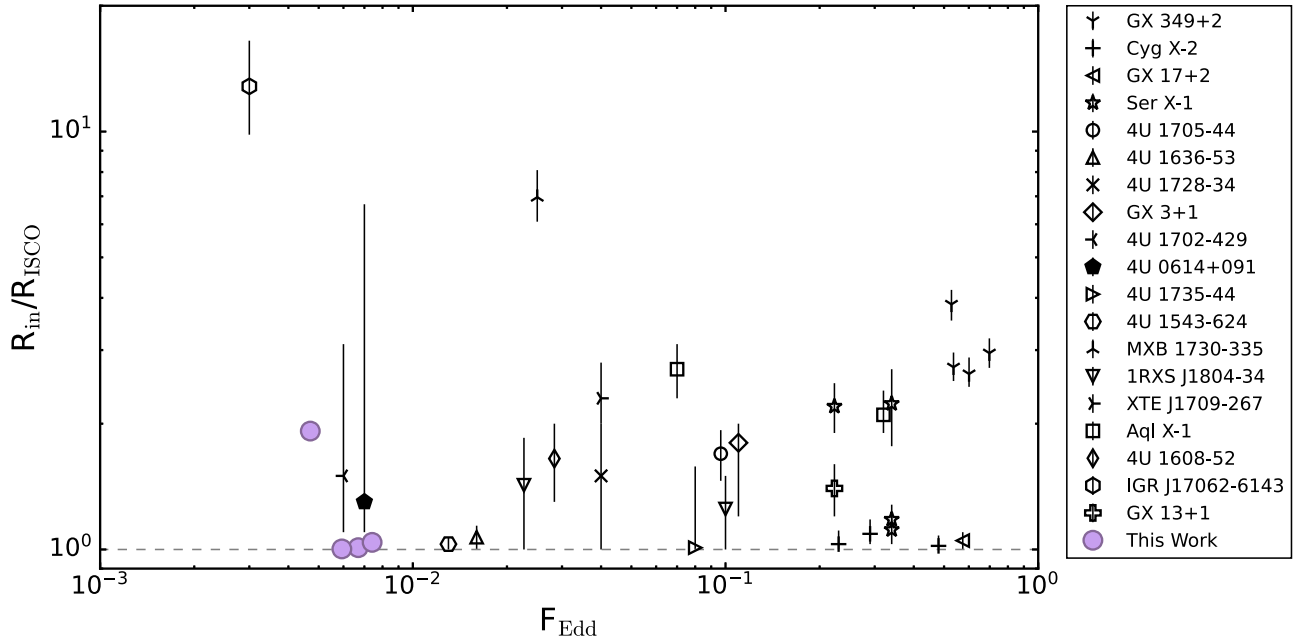

Figure 5. Eddington fraction $F_{\rm Edd}$ and the location of the inner disk as measured for several NS LMXBs studied with NuSTAR, and compared to this work. The Eddington fraction is the given luminosity of the source compared to the empirical Eddington luminosity for an NS. We see that there is almost no correlation between $F_{\rm Edd}$ and the inner disk radius, which differs from the more rigid correlation seen in BH LMXBs. A previous measurement of $R_{\rm in}$ from reflection modeling of NuSTAR data for this source is filled in black.

the reflected flux and the power-law flux may seem contrary. Here we provide two potential explanations for this:

1. XILLVERCO is a stand-alone reflection table, hence it does not simultaneously model the input continuum component and emergent reprocessed emission. We are utilizing a simple power-law component in the continuum and tie the photon index of the reflected emission to it in order to account for the incident flux, then broadening the features of XILLVERCO using RELCONV. This could lead to potential degeneracy between the reflected emission and the incident emission or with the thermal components, leading to some skewing of the relative contributions of each component. However, we believe the overall trends hold true given that if the relative contributions were skewed due to some degeneracy between model components, then they are likely skewed in the same manner given the uniform construct of our spectral modeling.
2. On the other hand, we can point to the truncation of the disk in observation 3 as a potential explanation for the observed reduction of the reflected flux. If the disk recedes from the compact object (and by extension the illuminating corona, assuming the corona is near the compact object and not the disk itself), we expect a reduction in the reflected flux as well. This does not account for the fact that there seems to be a negative correlation between the power-law flux and the flux of the reflected emission. However, as shown in Figure 6, for all but the highest power-law flux, the reflected flux is consistent within the 90% uncertainty.

We can compare our results to those of Koliopanos et al. (2014), who model the spectrum of 4U 0614+091 using only an absorbed power law plus a Gaussian to account for the bright O VIII reflection feature. We find a slightly lower power-law index reported than what is reported in this study, but our values are comparable (~ 2 in our analysis as opposed to 2.3 in theirs). We may account for this difference by noting that Koliopanos et al. (2014) use XMM-Newton, which is less sensitive in the harder X-ray regime, and the models used therein do not account for low-temperature thermal radiation, which could lead to a steeper power law. Their model also does not account for the full reflection spectrum and only includes a single feature to represent the reprocessed emission. This source was also characterized previously using XILLVERCO. Madej et al. (2014) find a value for the power-law index to be slightly higher than ours, again finding $\Gamma \approx 2.2$. They also found that both their disk and blackbody temperatures were slightly higher than ours. This could be due to the fact that Madej et al. were using a different absorption component in their model. Their measured values of $A_{\rm CO}$ are also significantly higher than the values we report. This is because, at the time of their analysis, Madej et al. were using an earlier version of XILLVERCO that had a different initial chemical composition grid, as discussed in Ludlam et al. (2021). The remainder of the parameters in XILLVERCO are comparable with our results. In that study, they also model the spectrum of a different UCXB, 4U 1543−624. The measured values of the disk temperature for that source are very close to what is seen in our analysis of 4U 0614+091 ($\sim$0.42 keV), but their blackbody temperatures are significantly lower, indicating that these sources can be variable.

5. Summary and Conclusions

We have studied four simultaneous NICER and NuSTAR observations of the UCXB 4U 0614+091 in an effort to track changes in the accretion disk as the system varies in flux. We modeled the spectra by combining a three-component continuum model with a relativistically broadened reflection component from XILLVERCO. Our results can be summarized as follows:

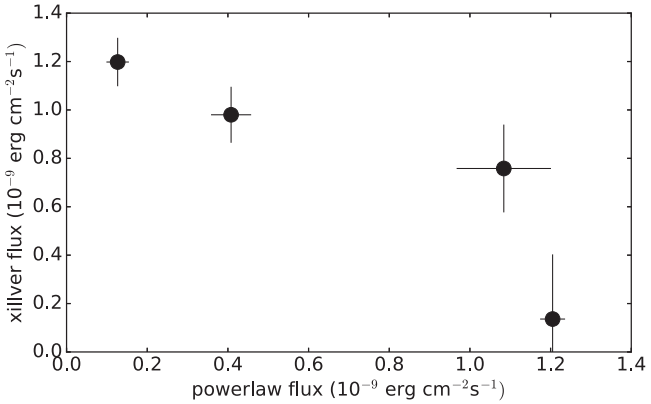

Figure 6. The plot above demonstrates that while there appears to be some negative correlation between the flux of the power-law component and the flux of the reflected emission, the 90% error bars show that across all observations except observation 3, which is the right-most point, the reflected emission is relatively consistent.

1. The flux of the reflected emission, as well as the flux of the thermal components representing emission from the accretion disk and the compact object itself, trend positively with the overall flux of the system.
2. The flux of the power-law component, representing the emission from the corona, trends in the opposite direction. As the flux of the system decreases and reaches its lowest point, the emission from this power-law component is at its maximum. This is consistent with the low/hard state seen in BH LMXBs.
3. During this low/hard state, we measure a slight disk truncation, with the inner disk being located close to $2\,R_{\rm ISCO}$. This disk truncation is analogous to what is seen in BH LMXB systems, where below a certain Eddington ratio, the spectrum hardens and the disk recedes. We discuss other scenarios, but it is unclear with the current data set what the physical process driving this truncation is.
4. We find that when the flux of the illuminating component (corona) is maximal, we see the minimum amount of reflected emission. A truncated disk can explain this discrepancy since the inner disk is further from the illuminating corona. There may be some uncertainty in the contributions of the various components due to some model degeneracies, but the trends are consistent across all observations and with previous studies of similar sources.

Our data set only covers roughly half a period of the flux variation, so drawing conclusions about the long-term behavior of this source is difficult. Future observations are needed to completely understand what the driver of flux variation is, as well as to understand the truncation of the accretion disk and its relation to the spectral state of the source. Future missions such as Athena (Nandra et al. 2013), or probe class concept missions, such as HEX-P (Madsen et al. 2019) or STROBE-X (Ray et al. 2018), could contribute immensely to such a study of the source by providing a broad X-ray passband, a larger effective collecting area, and/or higher energy resolution spectra. A deeper analysis of the faint Fe Kα with higher energy resolution instruments could provide tighter constraints on the location of the inner disk and could help to strengthen the idea that both the Fe K and O VIII features arise in the same location of the disk.

Acknowledgments

We thank the anonymous referee for the feedback, which improved the quality of the manuscript. This research has made use of data and/or software provided by the High Energy Astrophysics Science Archive Research Center (HEASARC), which is a service of the Astrophysics Science Division at NASA/GSFC. This research has also made use of the NuSTAR Data Analysis Software (NuSTARDAS) jointly developed by the ASI Science Data Center (ASDC, Italy) and the California Institute of Technology (USA). This work is supported by NASA under grant No. 80NSSC22K0054.

ORCID iDs

D. L. Moutard https://orcid.org/0000-0003-1463-8702
R. M. Ludlam https://orcid.org/0000-0002-8961-939X
J. A. García https://orcid.org/0000-0003-3828-2448
D. Altamirano https://orcid.org/0000-0002-3422-0074
E. M. Cackett https://orcid.org/0000-0002-8294-9281
J. Chenevez https://orcid.org/0000-0002-4397-8370
N. Degenaar https://orcid.org/0000-0002-0092-3548
A. C. Fabian https://orcid.org/0000-0002-9378-4072
J. Homan https://orcid.org/0000-0001-8371-2713
A. Jaodand https://orcid.org/0000-0002-3850-6651
S. N. Pike https://orcid.org/0000-0002-8403-0041
A. W. Shaw https://orcid.org/0000-0002-8808-520X
T. E. Strohmayer https://orcid.org/0000-0001-7681-5845
J. A. Tomsick https://orcid.org/0000-0001-5506-9855
B. M. Coughenour https://orcid.org/0000-0003-0870-6465

References

Arnason, R. M., Papei, H., Barmby, P., et al. 2021, MNRAS, 502, 5455
Arnaud, K. A. 1996, in ASP Conf. Ser. 101, Astronomical Data Analysis Software and Systems V, ed. G. H. Jacoby & J. Barnes (San Francisco, CA: ASP), 17
Brandt, S., Castro-Tirado, A. J., Lund, N., et al. 1992, A&A, 262, L15
Cackett, E. M., Altamirano, D., Patruno, A., et al. 2009b, ApJL, 694, L21
Cackett, E. M., Miller, J. M., Ballantyne, D. R., et al. 2010, ApJ, 720, 205
Cackett, E. M., Miller, J. M., Bhattacharyya, S., et al. 2008, ApJ, 674, 415
Chen, W. C., Liu, D. D., & Wang, B. 2020, ApJL, 900, L8
Chiang, C. Y., Morgan, R. A., Cackett, E. M., et al. 2016, ApJ, 831, 45
Christian, D. J., White, N. E., & Swank, J. H. 1994, ApJ, 422, 791
Churazov, E., Gilfanov, M., Forman, W., et al. 1996, ApJ, 471, 673
Dauser, T., García, J., Walton, D. J., et al. 2016, A&A, 590, A76
Done, C., Gierliński, M., & Kubota, A. 2007, A&ARv, 15, 1
Fabian, A. C., Rees, M. J., Stella, L., & White, N. E. 1989, MNRAS, 238, 729
Frank, J., King, A., & Raine, D. J. 2002, in Accretion Power in Astrophysics, ed. J. Frank, A. King, & D. J. Raine (Cambridge: Cambridge Univ. Press), 398
Galloway, D. K. 2020, ApJS, 249, 32
García, J., Dauser, T., Reynolds, C. S., et al. 2013, ApJ, 768, 146
García, J., & Kallman, T. R. 2010, ApJ, 718, 695
Gendreau, K. C., Arzoumanian, Z., & Okajima, T. 2012, Proc. SPIE, 8443, 13
Harrison, F. A., Craig, W. W., Christensen, F. E., et al. 2013, ApJ, 770, 103
Ibragimov, A., Poutanen, J., Gilfanov, M., et al. 2005, MNRAS, 362, 1435
Juett, A. M., Psaltis, D., & Chakrabarty, D. 2001, ApJL, 560, L59
Kaastra, J. S., & Bleeker, J. A. M. 2016, A&A, 587, A151
Koliopanos, F., Gilfanov, M., Bildsten, L., et al. 2014, in The X-ray Universe 2014, ed. J.-U. Ness, 102
Kuulkers, E., den Hartog, P. R., in't Zand, J. J. M., et al. 2003, A&A, 399, 663
Lazar, H., Tomsick, J. A., Pike, S. N., et al. 2021, ApJ, 921, 155
Liu, B. F., Yuan, W., Meyer, F., et al. 1999, ApJL, 527, L17
Ludlam, R. M., Cackett, E. M., García, J. A., et al. 2020, ApJ, 895, 45
Ludlam, R. M., Jaodand, A. D., García, J. A., et al. 2021, ApJ, 911, 123
Ludlam, R. M., Miller, J. M., Barret, D., et al. 2019, ApJ, 873, 99

Madej, O. K., García, J., Jonker, P. G., et al. 2014, MNRAS, 442, 1157
Madej, O. K., Jonker, P. G., Fabian, A. C., et al. 2010, MNRAS, 407, L11
Madsen, K., Hickcox, R., Bachetti, M., et al. 2019, BAAS, 51, 166
Marino, A., Malzac, J., Del Santo, M., et al. 2020, MNRAS, 498, 3351
Migliari, S., Tomsick, J. A., Miller-Jones, J. C. A., et al. 2010, ApJ, 710, 117
Miller, J. M. 2007, ARA&A, 45, 441
Mondal, A. S., Dewangan, G. C., & Raychaudhuri, B. 2020, MNRAS, 494, 3177
Nandra, K., Barret, D., Barcons, X., et al. 2013, arXiv:1306.2307
Nelemans, G., Jonker, P. G., Marsh, T. R., & van der Klis, M. 2004, MNRAS, 348, L7
Nelemans, G., Jonker, P. G., & Steeghs, D. 2006, MNRAS, 370, 255
Nelson, L. A., Rappaport, S. A., & Joss, P. C. 1986, ApJ, 304, 231
Ray, P. S., Arzoumanian, Z., Brandt, S., et al. 2018, Proc. SPIE, 10699, 1069919
Remillard, R. A., Loewenstein, M., Steiner, J. F., et al. 2022, AJ, 163, 130
Saavedra, E. A., García, F., Fogantini, F. A., et al. 2023, MNRAS, 522, 3367
Savonije, G. J., de Kool, M., & van den Heuvel, E. P. J. 1986, A&A, 155, 51
Shahbaz, T., Watson, C. A., Zurita, C., et al. 2008, PASP, 120, 848
Shimura, T., & Takahara, R. 1995, ApJ, 445, 780
Steiner, J. F., McClintock, J. E., Remillard, R. A., et al. 2010, ApJL, 718, L117
Steiner, J. F., Narayan, R., McClintock, J. E., & Ebisawa, K. 2009, PASP, 121, 1279
Swank, J. H., Becker, R. H., Boldt, E. A., et al. 1978, MNRAS, 182, 349
Syunyaev, R. A., Arefev, V. A., Borozdin, K. N., et al. 1991, SvAL, 17, 409
Tomsick, J. A., Yamaoka, K., Corbel, S., et al. 2009, ApJL, 707, L87
Verner, D. A., Ferland, G. J., Korista, K. T., et al. 1996, ApJ, 465, 487
Wilms, J., Allen, A., & McCray, R. 2000, ApJ, 542, 914